

Mean field theory of weakly-interacting Rydberg polaritons in the EIT system based on the nearest-neighbor distribution

Shih-Si Hsiao¹, Ko-Tang Chen¹, and Ite A. Yu^{1,2,*}

¹*Department of Physics, National Tsing Hua University, Hsinchu 30013, Taiwan*

²*Center for Quantum Technology, Hsinchu 30013, Taiwan*

The combination of high optical nonlinearity in the electromagnetically induced transparency (EIT) effect and strong electric dipole-dipole interaction (DDI) among the Rydberg-state atoms can lead to important applications in quantum information processing and many-body physics. One can utilize the Rydberg-EIT system in the strongly-interacting regime to mediate photon-photon interaction or qubit-qubit operation. One can also employ the Rydberg-EIT system in the weakly-interacting regime to study the Bose-Einstein condensation of Rydberg polaritons. Most of the present theoretical models dealt with the strongly-interacting cases. Here, we consider the weakly-interacting regime and develop a mean field model based on the nearest-neighbor distribution. Using the mean field model, we further derive the analytical formulas for the attenuation coefficient and phase shift of the output probe field. The predictions from the formulas are consistent with the experimental data in the weakly-interacting regime, verifying the validity of our model. As the DDI-induced phase shift and attenuation can be seen as the consequences of elastic and inelastic collisions among particles, this work provides a very useful tool for conceiving ideas relevant to the EIT system of weakly-interacting Rydberg polaritons, and for evaluating experimental feasibility.

I. INTRODUCTION

The effect of electromagnetically induced transparency (EIT) involving Rydberg-state atoms is of great interest currently. The Rydberg-state atoms exhibit the strong electric dipole-dipole interaction (DDI) among each others [1–5]. On the other hand, the EIT effect not only provides high optical nonlinearity for the atom-light interaction, but also gives rise to slow, stored, and stationary light for long interaction time [6–14]. Thus, the combination of the strong DDI of Rydberg atoms and the high optical nonlinearity of EIT can efficiently mediate the interaction between photons via Rydberg polaritons in the dipole blockade regime, where the Rydberg polariton is the collective excitation involving the light and the atomic coherence between the ground and Rydberg states [15, 16]. The Rydberg-EIT mechanism can lead to the applications of quantum optics and quantum information processing [17–32].

To our knowledge, most of the present theoretical models dealt with the Rydberg-EIT system in the strongly-interacting regime, i.e., r_B^3 is comparable to r_a^3 , where r_B is the blockade radius and r_a is the half mean distance between Rydberg polaritons. In Ref. [17], J. D. Pritchard *et al.* utilized the N -atom model to analyze experiment phenomena of the optical nonlinearity and attenuation in the Rydberg-EIT system. In Ref. [18], D. Petrosyan *et al.* modeled the propagation of light field in strongly-interacting Rydberg-EIT media by considering the superatoms with the volume of the blockade sphere. In Ref. [19], A. V. Gorshkov *et al.* proposed a theory for the propagation of few-photon pulses in the system of strongly-interacting Rydberg polaritons. In Ref. [24],

M. Moos *et al.* utilized a one-dimensional model to describe the time evolution of Rydberg polaritons and analyze many-body phenomena in the strongly-interacting regime. In Ref. [28], J. Ruseckas *et al.* proposed a method to create two-photon states by making pairs of Rydberg atoms entangled during the storage.

In this article, we considered the weakly-interacting Rydberg-EIT system, and developed a mean field model to describe the attenuation and phase shift of the output probe field induced by the DDI effect. The Rydberg-EIT system is depicted in Fig. 1(a), and the weakly-interacting condition requires $r_B^3 \ll r_a^3$ [see Fig. 1(b)]. Under such condition, the system of Rydberg polaritons can be considered as nearly the ideal gas. Thus, the nearest-neighbor distribution (NND) shown by Ref. [33] is utilized in our model. The DDI-induced frequency shift between nonuniformly-distributed Rydberg excitations results in the effective phase shift and attenuation of light field. With the probability function of NND and the atom-light coupling equations of EIT system, we calculated the mean field results of transmission and phase shift spectra, and further derived the analytical formulas of the DDI-induced attenuation coefficient and phase shift. The theoretical predictions from the formulas are in good agreement with the experimental data in Ref. [34]. In the experiment of Ref. [34], we utilized the Rydberg state of a low principal number, the laser-cooled ensemble of a moderate atomic density, and the weak probe field of a low photon flux to make the mean number of Rydberg polaritons within the blockade sphere lower than 0.1. The good agreement verifies our model.

Rydberg polaritons are regarded as bosonic quasi-particles, and the DDI-induced phase shift and attenuation coefficient can infer the elastic and inelastic collision rates in the ensemble of these particles [35]. Weakly-interacting Rydberg polaritons assisted by a long interaction time of the EIT effect can be employed in the study

*Electronic address: yu@phys.nthu.edu.tw

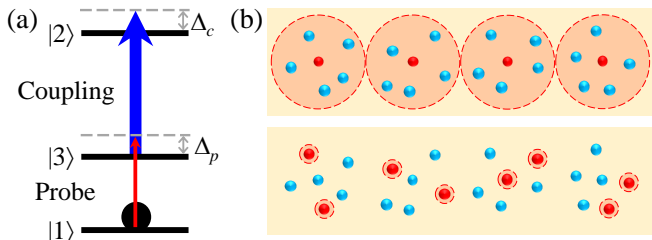


FIG. 1: (a) Transition diagram of the Rydberg-EIT system. $|1\rangle$, $|2\rangle$, and $|3\rangle$ represent the ground, Rydberg, and intermediate states. The weak probe and strong coupling fields form the ladder-type EIT configuration. (b) Top and bottom figures depict the strongly- and weakly-interacting systems. Red and blue balls represent the atoms with and without Rydberg excitations; dashed circles indicate the blockade spheres. As an example, let's consider 8 photons in both systems. There are 8 Rydberg excitations or polaritons in the weakly-interacting system, but only 4 in the strongly-interacting system due to the dipole blockade effect.

of many-body physics such as the Bose-Einstein condensation of polaritons [35–38]. The mean field theory developed in this work provides a useful tool to conceive ideas relevant to weakly-interacting EIT-based Rydberg polaritons and to evaluate feasibilities of experiments.

We organize the article as follows. In Sec. II, the theoretical model based on the probability function of NND, the atom-light coupling equations of the EIT system, and the ensemble average of the DDI-induced frequency shift are introduced. We obtain the mean field results of the real and imaginary parts of the steady-state absorption cross section of the probe field. In Sec. III, we numerically evaluate the integrals corresponding to the mean field results and present the spectra of transmission and phase shift of the output probe field. The DDI-induced phenomena observed from the spectra are discussed and explained. In Sec. IV, we derive the analytical formulas of the DDI-induced attenuation coefficient and phase shift. From the formulas, one can see how the DDI effects depend on the system parameters such as the optical depth, coupling and probe Rabi frequencies, coupling detuning, two-photon detuning, and decoherence rate. It is interesting to note that the DDI effects exhibit the asymmetric behavior with respect to the coupling detuning. In Sec. V, we briefly describe the experimental condition and data in Ref. [34], and calculate the predictions corresponding to the experimental condition from the analytical formulas. The predictions are in good agreement with the data. Finally, we give a summary in Sec. VI.

II. THEORETICAL MODEL

In the system of Rydberg polaritons, the DDI induces a frequency shift of the Rydberg state. Since Rydberg excitations are nonuniformly distributed, the Rydberg-state frequency shift is not a constant in the medium.

The system of low-density Rydberg excitations can be considered as the ideal gas, in which the nearest-neighbor distribution is given by [33]

$$P(r) = \frac{3r^2}{r_a^3} e^{-r^3/r_a^3}, \quad (1)$$

where $P(r)$ is the probability density, i.e., $P(r)dr$ is the probability of finding a particle's nearest neighbor locating at the distant between r and $r+dr$, and r_a is the half mean distance between particles. The definition of r_a is

$$r_a \equiv \left(\frac{3}{4\pi n_R} \right)^{1/3}, \quad (2)$$

where n_R is the Rydberg-polariton density. Figure 2(a) shows $P(r)$ as a function of r .

The frequency shift of a Rydberg state induced by the DDI is C_6/r^6 , where C_6 is the van der Waals coefficient [39] and r represents the distance between two particles. In the ensemble of Rydberg excitations, the Rydberg-state frequency shift consists of two parts. The first part is C_6/r^6 contributed from the nearest-neighbor Rydberg excitation at the distance r , and the second part is $n_R \int_r^\infty (C_6/r'^6) 4\pi r'^2 dr'$ contributed from all the other Rydberg excitations outside the sphere of the radius r . Here, we consider the particles in the second part are uniformly distributed. Thus, the Rydberg-state frequency shift is the following:

$$\omega = \frac{C_6}{r^6} + \frac{C_6}{r_a^3 r^3}. \quad (3)$$

Using Eqs. (1) and (3), we can obtain frequency shift distribution $P(\omega)$, i.e., $P(\omega)d\omega$ is the probability of finding the Rydberg-state frequency shifted by the amount between ω and $\omega+d\omega$, given by

$$P(\omega) = \frac{1}{\omega_a} \frac{\left[1 + \sqrt{1 + 4(\omega/\omega_a)} \right]^2}{4(\omega/\omega_a)^2 \sqrt{1 + 4(\omega/\omega_a)}} \times \exp \left[-\frac{1 + \sqrt{1 + 4(\omega/\omega_a)}}{2(\omega/\omega_a)} \right], \quad (4)$$

where

$$\omega_a \equiv |C_6|/r_a^6. \quad (5)$$

Since the value of distance, r , is always positive, only $\omega \geq 0$ is valid in $P(\omega)$. Figure 2(b) shows $P(\omega)$ as a function of ω .

We utilize the optical Bloch equation (OBE) for the time evolution of atomic density matrix and the Maxwell-Schrödinger equation (MSE) for the propagation of probe field in the theoretical model. In the EIT system here, the weak probe drives the transition between the ground state $|1\rangle$ and the intermediate state $|3\rangle$, and the strong coupling field drives that between $|3\rangle$ and the Rydberg

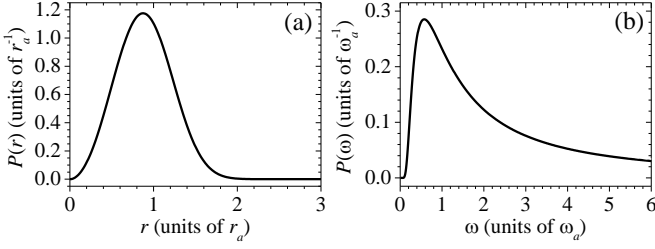


FIG. 2: (a) Probability density $P(r)$ as a function of distance r in the nearest-neighbor distribution. Units of r_a defined by Eq. (2) is the half mean distance between particles. (b) Probability density $P(\omega)$ as a function of frequency shift ω . Units of ω_a defined by Eq. (5) is the frequency shift corresponding to r_a .

state $|2\rangle$. The two transitions form the ladder configuration. The OBE and MSE are shown below.

$$\frac{\partial}{\partial t}\rho_{21} = \frac{i}{2}\Omega_c\rho_{31} + i\delta\rho_{21} - \left(\gamma_0 + \frac{\Gamma_2}{2}\right)\rho_{21}, \quad (6)$$

$$\frac{\partial}{\partial t}\rho_{31} = \frac{i}{2}\Omega_p + \frac{i}{2}\Omega_c\rho_{21} + i\Delta_p\rho_{31} - \frac{\Gamma}{2}\rho_{31}, \quad (7)$$

$$\frac{\partial}{\partial t}\rho_{22} = \frac{i}{2}\Omega_c\rho_{32} - \frac{i}{2}\Omega_c\rho_{32}^* - \Gamma_2\rho_{22}, \quad (8)$$

$$\begin{aligned} \frac{\partial}{\partial t}\rho_{32} &= \frac{i}{2}\Omega_p\rho_{21}^* + \frac{i}{2}\Omega_c(\rho_{22} - \rho_{33}) \\ &\quad - \left(\frac{\Gamma_2 + \Gamma}{2} + i\Delta_c\right)\rho_{32}, \end{aligned} \quad (9)$$

$$\begin{aligned} \frac{\partial}{\partial t}\rho_{33} &= -\frac{i}{2}\Omega_p^*\rho_{31} + \frac{i}{2}\Omega_p\rho_{31}^* - \frac{i}{2}\Omega_c\rho_{32} \\ &\quad + \frac{i}{2}\Omega_c\rho_{32}^* - \Gamma\rho_{33}, \end{aligned} \quad (10)$$

$$\frac{1}{c}\frac{\partial}{\partial t}\Omega_p + \frac{\partial}{\partial z}\Omega_p = i\frac{\alpha\Gamma}{2L}\rho_{31}, \quad (11)$$

where ρ_{ij} is the density matrix element between states $|i\rangle$ and $|j\rangle$, Ω_p and Ω_c represent the probe and coupling Rabi frequencies, Δ_p and Δ_c are the one-photon detunings of the probe and coupling transitions, $\delta = \Delta_p + \Delta_c$ is the two-photon detuning, γ_0 is the decoherence or dephasing rate of the Rydberg coherence ρ_{21} , Γ is the spontaneous decay rate of $|3\rangle$ which is $2\pi \times 6$ MHz in our case of the state $|5P_{3/2}\rangle$ of ^{87}Rb atoms, Γ_2 is the spontaneous decay rate of $|2\rangle$ which is $2\pi \times 5.4$ kHz in our case of the state $|32D_{5/2}\rangle$, and α and L are the optical depth (OD) and the length of the medium. Since $\Omega_p \ll \Omega_c$ and $\Omega_p \ll \Gamma$ in this work, we treat the probe field as a perturbation and keep only the terms of the lowest order of Ω_p in each equation. The value of Γ_2 is small and, thus, we set it to zero throughout this work.

We will determine the optical coherence, ρ_{31} , which is responsible for the attenuation coefficient and phase shift of the probe field. The steady-state solution is considered here and, hence, all the time-derivative terms are dropped in Eqs. (6)-(11). Equations (6) and (7) are used

to obtain the solution of ρ_{31} given by

$$\rho_{31}(\Delta_p, \Delta_c) = \frac{\Delta_p + \Delta_c + i\gamma_0}{\Omega_c^2/2 - 2(\Delta_p + i\Gamma/2)(\Delta_p + \Delta_c + i\gamma_0)}\Omega_p. \quad (12)$$

With above ρ_{31} , we solve Eq. (11) and find the ratio of output to input probe Rabi frequencies as the following:

$$\frac{\Omega_p(L)}{\Omega_p(0)} = \exp(i\phi - \beta/2), \quad (13)$$

where β and ϕ represent the attenuation coefficient and phase shift of the probe field at the output, and the probe transmission is $\exp(-\beta)$. We use β_0 and ϕ_0 to denote the attenuation coefficient and phase shift without the DDI effect. The optical coherence of the probe field determines β_0 and ϕ_0 as the followings:

$$\beta_0(\Delta_p, \Delta_c) = \alpha\Gamma \text{Im} \left[\frac{\rho_{31}(\Delta_p, \Delta_c)}{\Omega_p} \right], \quad (14)$$

$$\phi_0(\Delta_p, \Delta_c) = \frac{\alpha\Gamma}{2} \text{Re} \left[\frac{\rho_{31}(\Delta_p, \Delta_c)}{\Omega_p} \right]. \quad (15)$$

The effect of DDI on the attenuation coefficient and phase shift of the probe field will be derived in the following. Due to the DDI-induced frequency shift of the Rydberg state, the one-photon detuning of the coupling field transition is shifted by the amount of ω , i.e.,

$$\Delta_c \rightarrow \Delta_c \pm \omega.$$

Because $\omega \geq 0$, the positive or negative sign in the above corresponds to negative or positive C_6 , respectively, and we use $+\omega$ which corresponds to negative C_6 in the following. Under the DDI, the probe field propagates through the atoms with different DDI-induced frequency shifts, where the probability density $P(\omega)$ of the frequency shift distribution has been shown in Eq. (4). We obtain the values of β and ϕ by averaging ρ_{31} over the frequency distribution as shown below.

$$\beta(\Delta_p, \Delta_c) = \alpha\Gamma \int_0^\infty d\omega P(\omega) \text{Im} \left[\frac{\rho_{31}(\Delta_p, \Delta_c + \omega)}{\Omega_p} \right], \quad (16)$$

$$\phi(\Delta_p, \Delta_c) = \frac{\alpha\Gamma}{2} \int_0^\infty d\omega P(\omega) \text{Re} \left[\frac{\rho_{31}(\Delta_p, \Delta_c + \omega)}{\Omega_p} \right]. \quad (17)$$

The dipole blockade effect is that an atom inside the blockade sphere cannot be excited to the Rydberg state, where the blockade sphere centering with a Rydberg excitation has the radius $r_B \equiv (2C_6\Gamma/\Omega_c^2)^{1/6}$ [20]. This effect has already been included in the above formulas. In the weakly-interacting system considered here, i.e., $r_B^3 \ll r_a^3$, the average number of Rydberg excitations per volume of the blockade sphere is far less than one, and thus the dipole blockade appears rarely.

To evaluate Eqs. (16) and (17), one needs to know the value of ω_a in $P(\omega)$. According to the definition of ω_a in

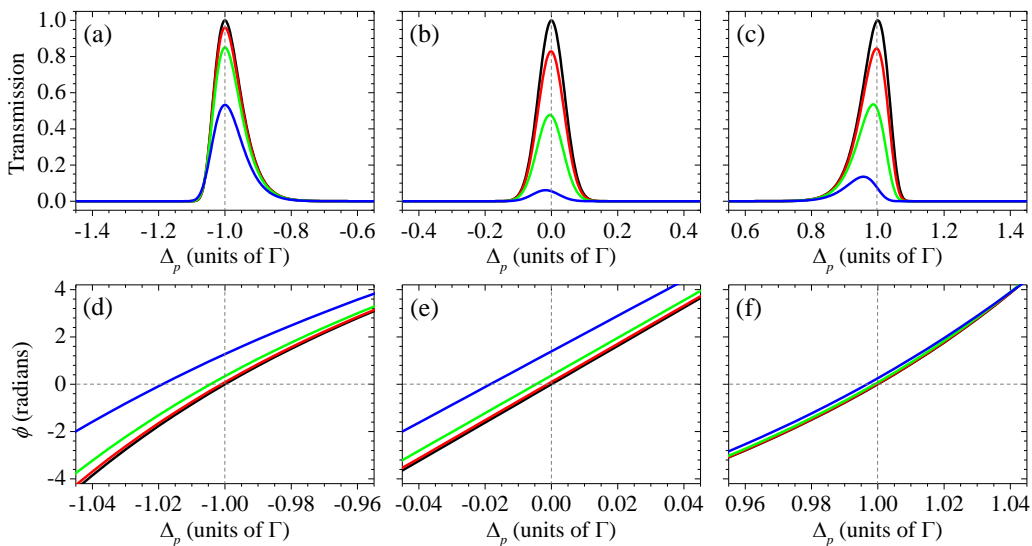


FIG. 3: (a-c) Transmissions of the probe field as functions of the probe detuning, Δ_p . (d-f) Phase shifts of the probe field as functions of Δ_p . The left two, middle two, and right two figures correspond to the coupling detunings, Δ_c , of $+1.0\Gamma$, 0 , and -1.0Γ , respectively. The vertical axes of the top three figures have the same scale, and those of the bottom three figures also have the same scale. Black lines represent predictions without DDI. Red, green, and blue lines represent predictions with DDI at $\Omega_{p,\text{in}} = 0.05\Gamma$, 0.1Γ , and 0.2Γ . All the predictions are calculated with $\alpha = 81$, $\Omega_c = 1.0\Gamma$, and $\gamma_0 = 0$ in Eqs. (16) and (17), and $|C_6|[(4\pi/3)n_{\text{atom}}\varepsilon]^2 = 0.35\Gamma$ in Eq. (18).

Eq. (5) and that of r_a in Eq. (2), we can relate ω_a to the Rydberg-polariton density, n_R , as $\omega_a = |C_6|[(4\pi/3)n_R]^2$. The product of the atomic density, n_{atom} , and the average Rydberg-state population, $\bar{\rho}_{22}$, gives n_R , and therefore $\omega_a = |C_6|[(4\pi/3)n_{\text{atom}}\bar{\rho}_{22}]^2$. The DDI-induced nonlinear and many-body effects make $\bar{\rho}_{22}$ no longer be the steady-state solution of the OBE shown in Eqs. (6)-(10). Nevertheless, one can phenomenologically associate $\bar{\rho}_{22}$ to the steady-state solution of Rydberg-state population at the input, $\rho_{22,\text{in}}$, by introducing a parameter ε . Substituting $\varepsilon\rho_{22,\text{in}}$ for $\bar{\rho}_{22}$, we obtain

$$\omega_a = |C_6|[(4\pi/3)n_{\text{atom}}\varepsilon\rho_{22,\text{in}}]^2, \quad (18)$$

where ε is the phenomenological parameter representing the average value of entire ensemble.

III. PREDICTIONS OF TRANSMISSION AND PHASE-SHIFT SPECTRA

The spectra of probe transmission and phase shift under the DDI effect are obtained by numerically evaluating the integrals of Eqs. (16) and (17) with the value of ω_a given by Eq. (18). Figures 3(a)-3(c) show the probe transmission versus the probe detuning at the coupling detunings of $+1\Gamma$, 0 , and -1Γ ; similarly, Figs 3(d)-3(e) show the probe phase shift. The spectra without and with the DDI are calculated with Eq. (14) [or Eq. (15)] and Eq. (16) [or Eq. (17)], respectively.

The DDI-induced phenomena exhibited in the transmission and phase shift spectra are summarized as follows: (1) A larger probe intensity results in a smaller

transmission or larger attenuation. (2) A larger probe intensity results in a larger phase shift at $\delta = 0$. (3) With the same probe intensity, the attenuation at a positive coupling detuning (e.g., $\Delta_c = +1\Gamma$) is smaller than that at a negative coupling detuning (e.g., $\Delta_c = -1\Gamma$), where the positive and negative detunings have the same magnitude. (4) With the same probe intensity, the phase shift at $\delta = 0$ of a positive coupling detuning (e.g., $\Delta_c = +1\Gamma$) is larger than that of a negative coupling detuning (e.g., $\Delta_c = -1\Gamma$), where the positive and negative detunings have the same magnitude. (5) The position of the EIT peak transmission at $\Delta_c = +1\Gamma$ changes very little and locates around $\delta = 0$; that at $\Delta_c = -1\Gamma$ shifts away from $\delta = 0$ significantly and a larger probe intensity induces a greater shift. We will explain the first four phenomena in the next three paragraphs and the last one in the Appendix.

First of all, the peak transmission decreases against the probe Rabi frequency [see Figs. 3(a), 3(b), and 3(c)]. This is expected, because the Rydberg-state population is proportional to the probe intensity or Rabi frequency square. A larger Rydberg-state population or Rydberg-polariton density makes ω_a larger as shown by Eq. (18). The probability density $P(\omega)$ with the larger ω_a has a broader width and a longer tail as demonstrated by Fig. 2(b). Under the broader $P(\omega)$, more atoms have the Rydberg-state frequency shifted away from the EIT resonance condition, reducing the peak transmission more. Secondly, the phase shift increases against the probe Rabi frequency [see Figs. 3(d), 3(e), and 3(f)]. The explanation is similar to that in the first phenomenon.

The third phenomenon observed in the spectra is that

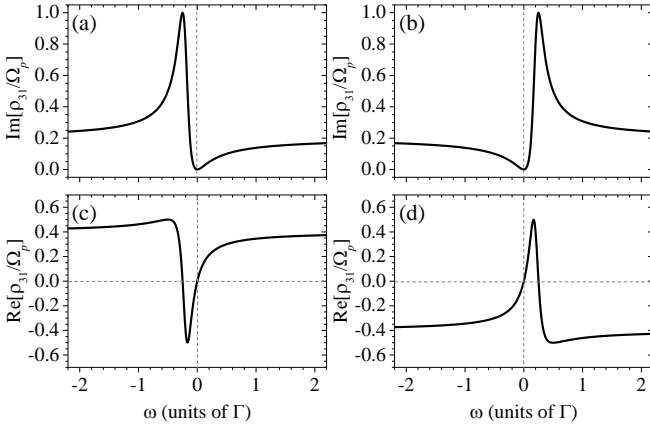


FIG. 4: The imaginary and real parts of ρ_{31}/Ω_p as functions of the frequency shift ω , calculated with Eq. (12) in which we make the substitution of $\Delta_c \rightarrow \Delta_c + \omega$ and $\Delta_p \rightarrow -\Delta_c$. In the calculation, $\Omega_c = 1.0\Gamma$, $\gamma_0 = 0$, $\delta = 0$, and $\Delta_c = 1.0\Gamma$ in (a,c) and -1.0Γ in (b,d).

the probe intensity or $\Omega_{p,\text{in}}^2$ has a smaller effect on the reduction of peak transmission at $\Delta_c = +1\Gamma$ as shown by Fig. 3(a) than that at $\Delta_c = -1\Gamma$ as shown by Fig. 3(c). This can be explained with the help of Figs. 4(a) and 4(b), which show $\text{Im}[\rho_{31}/\Omega_p]$ at $\Delta_c = 1\Gamma$ and -1Γ , respectively. To obtain the probe transmission, the integration of Eq. (16) is performed only for the region of $\omega > 0$. In Fig. 4(a), the value of $\text{Im}[\rho_{31}/\Omega_p]$ is always small for $\omega > 0$, resulting in a smaller value of $\int_0^\infty d\omega P(\omega)\text{Im}[\rho_{31}/\Omega_p]$, i.e., a higher probe transmission. On the other hand, in Fig. 4(b), the value of $\text{Im}[\rho_{31}/\Omega_p]$ has a large peak for $\omega > 0$, which corresponds to the absorption due to the two-photon transition. This large peak results in a larger value of $\int_0^\infty d\omega P(\omega)\text{Im}[\rho_{31}/\Omega_p]$, i.e., a lower probe transmission. Therefore, with the same value of $\Omega_{p,\text{in}}$, the peak transmission at $\Delta_c = 1\Gamma$ shown by Fig. 3(a) is larger than that at $\Delta_c = -1\Gamma$ shown by Fig. 3(c).

The fourth phenomenon observed in the spectra is that the probe intensity or $\Omega_{p,\text{in}}^2$ has a much larger effect on the phase shift of $\delta = 0$ at $\Delta_c = 1\Gamma$ as shown by Fig. 3(d) than that at $\Delta_c = -1\Gamma$ as shown by Fig. 3(f). This can be explained with the help of Figs. 4(c) and 4(d), which show $\text{Re}[\rho_{31}/\Omega_p]$ at $\Delta_c = 1\Gamma$ and -1Γ , respectively. To obtain the phase shift, the integration of Eq. (17) is performed only for the region of $\omega > 0$. In Fig. 4(c), the value of $\text{Re}[\rho_{31}/\Omega_p]$ is always positive for $\omega > 0$, resulting in a larger value of $\int_0^\infty d\omega P(\omega)\text{Re}[\rho_{31}/\Omega_p]$, i.e., a larger phase shift. On the other hand, in Fig. 4(d), $\text{Re}[\rho_{31}/\Omega_p]$ has both positive and negative values for $\omega > 0$, because the resonance of the two-photon transition locates at $\omega > 0$. The cancellation between positive and negative values of the integrand makes $\int_0^\infty d\omega P(\omega)\text{Re}[\rho_{31}/\Omega_p]$ nearly zero, i.e., almost no phase shift. Therefore, with the same value of $\Omega_{p,\text{in}}$, the phase shift at $\Delta_c = 1\Gamma$ shown by Fig. 3(d) is significant, and that at $\Delta_c = -1\Gamma$ shown

by Fig. 3(f) is little.

IV. ANALYTICAL FORMULAS OF THE DDI-INDUCED ATTENUATION COEFFICIENT AND PHASE SHIFT

We now derive the analytical formulas for the DDI-induced attenuation coefficient, $\Delta\beta$, and phase shift, $\Delta\phi$, at the condition of $\gamma_0 = 0$ and $\delta = 0$ (or $\Delta_p = -\Delta_c$). Here, $\Delta\beta$ (or $\Delta\phi$) is defined as the difference between the values of β (or ϕ) with and without the DDI effect, i.e., $\Delta\beta \equiv \beta - \beta_0$ and $\Delta\phi \equiv \phi - \phi_0$.

At $\gamma_0 = 0$ and $\delta = 0$, Eq. (12) gives $\beta_0 = 0$ and $\phi_0 = 0$, and thus $\Delta\beta = \beta$ and $\Delta\phi = \phi$. Replacing Δ_p by $-\Delta_c$ in β of Eq. (16) and in ϕ of Eq. (17), we obtain $\Delta\beta$ and $\Delta\phi$ as follows:

$$\Delta\beta = \alpha\Gamma \int_0^\infty d\omega P(\omega) \frac{4\omega^2\Gamma}{4\omega^2\Gamma^2 + (4\omega\Delta_c + \Omega_c^2)^2}, \quad (19)$$

$$\Delta\phi = \frac{\alpha\Gamma}{2} \int_0^\infty d\omega P(\omega) \frac{8\omega^2\Delta_c + 2\omega\Omega_c^2}{4\omega^2\Gamma^2 + (4\omega\Delta_c + \Omega_c^2)^2}. \quad (20)$$

In the weakly-interacting or low-density system, the region of ω being the order of ω_a is very near the center of the EIT window, in which $\text{Im}[\rho_{31}/\Omega_p]$ and $\text{Re}[\rho_{31}/\Omega_p]$ are nearly zero and contribute to the above two integrals very little. On the other hand, the region of $\omega \gg \omega_a$ is away from the center of the EIT window, and contributes to the above two integrals predominately. Under $\omega \gg \omega_a$, in the integrands of Eqs. (19) and (20) we can make the approximation of $P(\omega)$ as

$$P(\omega) \approx \frac{\sqrt{\omega_a}}{2\omega^{3/2}} \equiv P'(\omega), \quad (21)$$

where ω_a is given by Eq. (18). In Eq. (18), the steady-state solution of $\rho_{22,\text{in}}$ is

$$\rho_{22,\text{in}} = \frac{\Omega_{p,\text{in}}^2 \Omega_c^2}{4\delta^2\Gamma^2 + (\Omega_c^2 - 4\delta\Delta_p)^2} \approx \frac{\Omega_{p,\text{in}}^2}{\Omega_c^2}, \quad (22)$$

where $\delta\Gamma, \delta\Delta_p \ll \Omega_c^2$ is the typical condition in most of the EIT experiments. Without any other approximation, we use $P'(\omega)$ in Eqs. (19) and (20) and replace $\rho_{22,\text{in}}$ in ω_a by $\Omega_{p,\text{in}}^2/\Omega_c^2$ to obtain

$$\Delta\beta = 2S_{\text{DDI}} \sqrt{\frac{W_c - 2\Delta_c}{W_c^2}} \Omega_{p,\text{in}}^2, \quad (23)$$

$$\Delta\phi = S_{\text{DDI}} \sqrt{\frac{W_c + 2\Delta_c}{W_c^2}} \Omega_{p,\text{in}}^2, \quad (24)$$

where

$$S_{\text{DDI}} \equiv \frac{\pi^2\alpha\Gamma\sqrt{C_6}n_{\text{atom}}\varepsilon}{3\Omega_c^3}, \quad (25)$$

$$W_c \equiv \sqrt{\Gamma^2 + 4\Delta_c^2}. \quad (26)$$

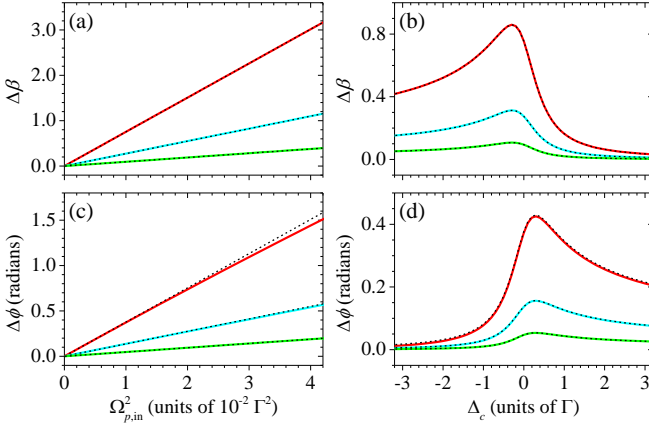


FIG. 5: (a,c) The DDI-induced attenuation coefficient $\Delta\beta$ and phase shift $\Delta\phi$ as functions of $\Omega_{p,\text{in}}^2$ under $\Delta_p = \Delta_c = 0$. (b,d) $\Delta\beta$ and $\Delta\phi$ as functions of Δ_c under $\delta = 0$ and $\Omega_{p,\text{in}} = 0.1\Gamma$. The horizontal axes of the left two figures have the same scale, so do those of the right two figures. Red, cyan, and green solid lines represent the numerical evaluations of the integrals in Eqs. (19) and (20) at $\Omega_c = 1.0\Gamma$, 1.4Γ , and 2.0Γ . Dashed lines are the results of the analytical formulas given by Eqs. (23) and (24). All the predictions are calculated with $\alpha = 81$, $\gamma_0 = 0$, and $|C_6|[(4\pi/3)n_{\text{atom}}\varepsilon]^2 = 0.35\Gamma$.

The above results being good approximations imposes the condition that ω_a is much smaller than the EIT linewidth, $\Delta\omega_{\text{EIT}}$, where $\Delta\omega_{\text{EIT}} = \Omega_c^2 \sqrt{\Gamma^2 + 8\Delta_c^2}/(\Gamma^2 + 4\Delta_c^2)$ derived from the spectrum of $\text{Im}[\rho_{31}(\omega)]$ at $\delta = 0$. More precisely, the accuracy of the analytical formula of $\Delta\beta$ requires $(\omega_a/\Delta\omega_{\text{EIT}})^{3/2} \ll 1$, and that of $\Delta\phi$ requires $(\omega_a/\Delta\omega_{\text{EIT}})^{1/2} \ll 1$.

In Fig. 5, we compare the results of the above two analytical formulas with those of the numerical integrations of Eqs. (19) and (20) without the approximation of $P(\omega)$. The agreement between the results of the analytical formulas and numerical integrations is satisfactory except the line of $\Delta\phi$ at $\Omega_c = 1.0\Gamma$ in the region of $\Omega_{p,\text{in}}^2 > 0.02\Gamma^2$. In this region, $(\omega_a/\Delta\omega_{\text{EIT}})^{1/2} \ll 1$ is no longer well satisfied, and the deviation between the analytical formula and the numerical integration becomes observable. Figures 5(a) and 5(c) demonstrate that both of $\Delta\beta$ and $\Delta\phi$ are proportional to $\Omega_{p,\text{in}}^2/\Omega_c^3$. Figure 5(b) [or 5(d)] shows the asymmetric phenomenon that the value of $\Delta\beta$ (or $\Delta\phi$) at the coupling detuning of $|\Delta_c|$ is smaller (or larger) than that at the coupling detuning of $-|\Delta_c|$.

In reality, there exist a nonzero decoherence rate γ_0 and the two-photon detuning δ in the system. We need to consider the corrections of γ_0 and δ to the analytical formulas. Under the condition of $\Omega_c^2 \gg \gamma_0\Gamma, \delta\Gamma$, the attenuation coefficient and phase shift without the DDI effect, β_0 and ϕ_0 , are approximately given by

$$\beta_0 \approx \frac{2\alpha\gamma_0\Gamma}{\Omega_c^2} - \frac{16\alpha\gamma_0\delta\Delta_c\Gamma}{\Omega_c^4}, \quad (27)$$

$$\phi_0 \approx \frac{\alpha\Gamma\delta}{\Omega_c^2} - \frac{4\alpha\gamma_0\delta\Gamma^2}{\Omega_c^4} + \frac{4\alpha(\gamma_0^2 - \delta^2)\Delta_c\Gamma}{\Omega_c^4}. \quad (28)$$

To derive the DDI-induced attenuation coefficient, $\Delta\beta$, and phase shift, $\Delta\phi$, we first use the replacement of $\Delta_c \rightarrow \Delta_c + \omega$ and the relation of $\delta = \Delta_p + \Delta_c$ in ρ_{31}/Ω_p shown by Eq. (12). Then, we expand ρ_{31}/Ω_p with respect to γ_0 and δ under the assumption of $\Omega_c^2/\Gamma \gg \gamma_0, \delta$ to obtain

$$\text{Im}\left[\frac{\rho_{31}}{\Omega_p}\right] = A_0 + A_1\gamma_0 + A_2\delta + \dots, \quad (29)$$

$$\text{Re}\left[\frac{\rho_{31}}{\Omega_p}\right] = B_0 + B_1\gamma_0 + B_2\delta + \dots, \quad (30)$$

where

$$A_0 = \frac{4\omega^2\Gamma}{4\omega^2\Gamma^2 + (4\omega\Delta_c + \Omega_c^2)^2}, \quad (31a)$$

$$A_1 = \frac{2\Omega_c^2[(4\omega^2\Delta_c + \Omega_c^2)^2 - 4\omega^2\Gamma^2]}{[4\omega^2\Gamma^2 + (4\omega\Delta_c + \Omega_c^2)^2]^2}, \quad (31b)$$

$$A_2 = \frac{8\omega\Gamma\Omega_c^2(4\Delta_c\omega + \Omega_c^2)}{[4\omega^2\Gamma^2 + (4\omega\Delta_c + \Omega_c^2)^2]^2}, \quad (31c)$$

and

$$B_0 = \frac{8\Delta_c\omega^2 + 2\omega\Omega_c^2}{4\omega^2\Gamma^2 + (4\omega\Delta_c + \Omega_c^2)^2}, \quad (32a)$$

$$B_1 = -\frac{8\omega\Gamma\Omega_c^2(4\Delta_c\omega + \Omega_c^2)}{[4\omega^2\Gamma^2 + (4\omega\Delta_c + \Omega_c^2)^2]^2}, \quad (32b)$$

$$B_2 = \frac{2\Omega_c^2[(4\omega^2\Delta_c + \Omega_c^2)^2 - 4\omega^2\Gamma^2]}{[4\omega^2\Gamma^2 + (4\omega\Delta_c + \Omega_c^2)^2]^2}. \quad (32c)$$

Next, we evaluate the two integrals of Eqs. (16) and (17) by substituting Eqs. (29) and (30) for $\text{Im}[\rho_{31}/\Omega_p]$ and $\text{Re}[\rho_{31}/\Omega_p]$ in the integrands. Since ω_a is much less than the EIT linewidth, $P'(\omega)$ shown in Eq. (21) can be employed in Eqs. (16) and (17) to replace $P(\omega)$. The results of the two integrals give β and ϕ . Finally, the analytical formulas of $\Delta\beta (= \beta - \beta_0)$ and $\Delta\phi (= \phi - \phi_0)$, including the corrections of γ_0 and δ are given by

$$\Delta\beta = 2S_{\text{DDI}} \left(\sqrt{\frac{W_c - 2\Delta_c}{W_c^2}} - \frac{3\gamma_0\sqrt{W_c + 2\Delta_c}}{\Omega_c^2} + \frac{3\delta\sqrt{W_c - 2\Delta_c}}{\Omega_c^2} \right) \Omega_{p,\text{in}}^2, \quad (33)$$

$$\Delta\phi = S_{\text{DDI}} \left(\sqrt{\frac{W_c + 2\Delta_c}{W_c^2}} - \frac{3\gamma_0\sqrt{W_c - 2\Delta_c}}{\Omega_c^2} - \frac{3\delta\sqrt{W_c + 2\Delta_c}}{\Omega_c^2} \right) \Omega_{p,\text{in}}^2. \quad (34)$$

Regarding $\Delta\beta$ as a function of $\Omega_{p,\text{in}}^2$ in Fig. 5(a), the slope will decrease a little due to γ_0 , and become a little larger (or smaller) due to positive (or negative) δ . Regarding $\Delta\phi$ as a function of $\Omega_{p,\text{in}}^2$ in Fig. 5(c), the slope will decrease a little due to γ_0 , and become a little smaller (or larger) due to positive (or negative) δ . When we consider β and ϕ instead of $\Delta\beta$ and $\Delta\phi$ in Figs. 5(a) and 5(c), β_0 and ϕ_0 make nonzero vertical-axis interceptions of those lines.

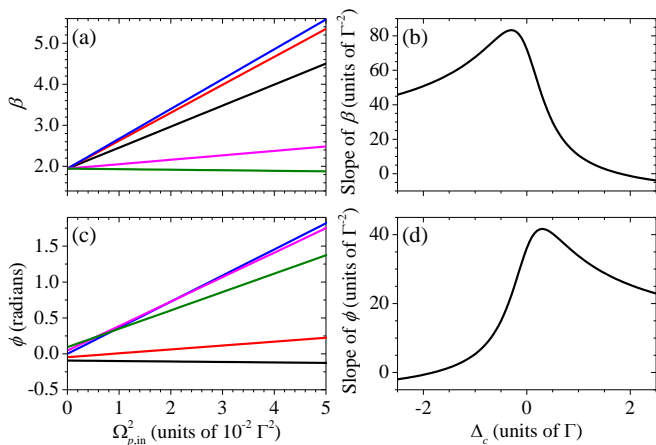


FIG. 6: Simulation of the experimental data shown in Fig. 2 of Ref. [34]. In the simulation, $\alpha = 81$, $\Omega_c = 1.0\Gamma$, $\delta = 0$, $\gamma_0 = 0.012\Gamma$, and $|C_6|[(4\pi/3)n_{\text{atom}}\varepsilon]^2 = 0.35\Gamma$. (a,c) Attenuation coefficient β and phase shift ϕ as functions of $\Omega_{p,\text{in}}^2$ at $\Delta_c = -2\Gamma$ (black), -1Γ (red), 0 (blue), 1Γ (magenta), and 2Γ (olive). (b,d) Slope of β versus $\Omega_{p,\text{in}}^2$ and that of ϕ versus $\Omega_{p,\text{in}}^2$ as functions of Δ_c .

V. SIMULATION OF THE EXPERIMENTAL DATA

To verify the mean field theory developed in this work, we systematically measured the attenuation coefficient, β , and phase shift, ϕ , of the output probe field as shown in Fig. 2 of Ref. [34]. The experiment was carried out in cold ^{87}Rb atoms with the temperature of $350 \mu\text{K}$. The ground state $|1\rangle$, Rydberg state $|2\rangle$, and excited state $|3\rangle$ in the EIT system here correspond to $|5S_{1/2}, F = 2, m_F = 2\rangle$, $|32D_{5/2}, m_J = 5/2\rangle$, and $|5P_{3/2}, F = 3, m_F = 3\rangle$ in the experiment. We set $\Omega_c = 1.0\Gamma$ and $\Omega_{p,\text{in}} \leq 0.2\Gamma$, and the atomic density was about $0.05 \mu\text{m}^{-3}$. Hence, the blockade radius $r_B = 2.1 \mu\text{m}$, and the half mean distance between Rydberg polaritons $r_a \geq 4.9 \mu\text{m}$. The weakly-interacting condition of $r_B^3 \ll r_a^3$ was satisfied in the measurement. Other experimental details can be found in Ref. [34].

In Fig. 6, we made the predictions with Eqs. (27), (28), (33), and (34) for the comparison with the experimental data in Fig. 2 of Ref. [34]. The calculation parameters of OD, coupling Rabi frequency, two-photon detuning, and decoherence rate were determined experimentally. As for the value of S_{DDI} , we used $C_6 = -2\pi \times 260 \text{ MHz} \cdot \mu\text{m}^6$ of the state $|32D_{5/2}, m_J = 5/2\rangle$, $n_{\text{atom}} = 0.05 \mu\text{m}^{-3}$ estimated from the experimental condition, and $\varepsilon = 0.43$ determined by the experimental data. Figures 6(a) and 6(c) show the attenuation coefficient, β , and phase shift, ϕ , of the output probe field as functions of $\Omega_{p,\text{in}}^2$, where $\Omega_{p,\text{in}}$ is the peak Rabi frequency of the Gaussian probe beam in the experiment. Figure 6(b) [or 6(d)] shows the slope of the straight line of β (or ϕ) versus $\Omega_{p,\text{in}}^2$ as a function of Δ_c . Note that the decoherence rate, γ_0 , of 0.012Γ makes the y -axis interception, i.e., β_0 or ϕ_0 ,

becomes nonzero according to Eqs. (27) and (28), and changes the slopes very little according to Eqs. (33) and (34).

In Fig. 2 of Ref. [34], the circles are the experimental data and the lines are their best fits. One can clearly observe the important characteristics of asymmetry in the data of slope versus Δ_c . The consistency between the theoretical predictions in Fig. 6 here and the data or best fits in Fig. 2 of Ref. [34] is satisfactory. The discrepancies in the y -axis interceptions of straight lines between the predictions and best fits are minor, and can be explained by the uncertainties or fluctuations of δ and γ_0 in the experiment. Therefore, the mean field theory developed in this work is confirmed by the experimental data.

VI. CONCLUSION

In summary, a mean field theory based on the nearest-neighbor distribution is developed to describe the DDI effect in the system of weakly-interacting EIT-Rydberg polaritons. Employing the theory, we numerically calculate the spectra of probe transmission and phase shift as shown in Fig. 3. We also explain the DDI-induced phenomena observed from the spectra. To make the theory convenient for predicting experimental outcomes and evaluating experimental feasibility, analytical formulas of the DDI-induced attenuation coefficient, $\Delta\beta$, and phase shift, $\Delta\phi$, are derived. As long as ω_a is much smaller than the EIT linewidth, the results of analytical formulas are in good agreement with those of numerical calculations. According to the formulas, $\Delta\beta$ and $\Delta\phi$ are linearly proportional to $\Omega_{p,\text{in}}^2$ as demonstrated in Fig. 5(a) and 5(c), and $\Delta\beta$ and $\Delta\phi$ as functions of Δ_c are asymmetric with respect to $\Delta_c = 0$ as demonstrated in Fig. 5(b) and 5(d). We further consider the existences of nonzero but small decoherence rate and two-photon detuning in the system, and make corrections to the formulas of $\Delta\beta$ and $\Delta\phi$ as shown in Eqs. (33) and (34). Finally, we make the predictions with the parameters determined experimentally and compare them with the experimental data in Ref. [34]. The good agreement between the predictions and data demonstrates the validity of our theory. Rydberg polaritons are regarded as bosonic quasi-particles, and the DDI is the origin of the interaction between the particles. Thus, the DDI-induced phase shift and attenuation coefficient can infer the elastic and inelastic collision rates in the ensemble of these bosonic particles. Our mean field theory provides a useful tool for conceiving ideas relevant to the EIT system of weakly-interacting Rydberg polaritons, and for evaluating experimental feasibility.

ACKNOWLEDGMENTS

This work was supported by Grant Nos. 107-2745-M-007-001 and 108-2639-M-007-001-ASP of the Ministry of

APPENDIX

The fifth phenomenon observed in the spectra as shown by Fig. 3 is that the DDI effect shifts the position of EIT peak transmission very little at $\Delta_c = 1\Gamma$ as shown by Fig. 3(a) and significantly at $\Delta_c = -1\Gamma$ as shown by Fig. 3(c). We will explain the phenomenon in this Appendix.

There are two effects associating with the phenomenon. The first effect relates to the decoherence rate. According to Eq. (12), at $\Delta_c \neq 0$ the decoherence rate causes the EIT peak position to shift from $\delta = 0$ to

$$\delta_{\text{peak},\gamma} = \frac{2\gamma\Delta_c}{\Gamma} \quad (\text{A1})$$

under the condition of $\Omega_c^2 \gg \gamma\Delta_c, \gamma\Gamma$, where γ here can be the intrinsic decoherence rate γ_0 , the DDI-induced decoherence rate γ_{eff} , or sum of the two rates. Since the DDI-induced attenuation at $\Delta_c = +1\Gamma$ is less than that at $\Delta_c = -1\Gamma$, the value of γ_{eff} in the former is smaller than that in the latter. Thus, according to Eq. (A1) the shift of the EIT peak position due to γ_{eff} at $\Delta_c = +1\Gamma$ (denoted $\delta_{\text{peak},\gamma,+}$) has a smaller magnitude than that at $\Delta_c = -1\Gamma$ (denoted $\delta_{\text{peak},\gamma,-}$), i.e. $|\delta_{\text{peak},\gamma,+}| < |\delta_{\text{peak},\gamma,-}|$ where $\delta_{\text{peak},\gamma,+} > 0$ and $\delta_{\text{peak},\gamma,-} < 0$.

The second effect relates to the phase shift at $\delta = 0$ (denoted as $\phi_{\delta=0}$). This nonzero $\phi_{\delta=0}$ implies that the position of EIT peak transmission is shifted from $\delta = 0$ to

$$\delta_{\text{peak},\phi} = -\frac{\phi_{\delta=0}}{\tau_d}, \quad (\text{A2})$$

where $\tau_d = \alpha\Gamma/\Omega_c^2$ is the propagation delay time. The

above equation shows the relation between the EIT peak position, $\delta_{\text{peak},\phi}$, and the DDI-induced phase shift at $\delta = 0$. Figures 3(b) and 3(e) demonstrate this relation. At $\Delta_c = 0$, γ_{eff} cannot cause the shift of EIT peak position because of Eq. (A1), but $\phi_{\delta=0}$ can. Thus, the position of the EIT peak transmission shifted away from $\delta = 0$ as shown by Fig. 3(b) must be due to $\phi_{\delta=0}$. In Fig. 3(e), the phase shift spectra behave nearly straight lines. The peak positions in the transmission spectra, i.e., $\delta_{\text{peak},\phi}$, of Fig. 3(b) approximately match the zero-crossing points of the corresponding straight lines in Fig. 3(e). In other words, the zero-crossing point is $\delta_{\text{peak},\phi}$. The slopes of these straight lines are equal to the propagation delay time (τ_d), i.e., $\tau_d = -\phi_{\delta=0}/\delta_{\text{peak},\phi}$ where $\phi_{\delta=0} > 0$ and $\delta_{\text{peak},\phi} < 0$. One can clearly see the relation of Eq. (A2) from Figs. 3(b) and 3(e).

Now, we use Eq. (A2) to determine the frequency shift of the EIT peak caused by the second effect. Since the value of $\phi_{\delta=0}$ in Fig. 3(d) is positive and significant, the shift of the EIT peak position due to $\phi_{\delta=0}$ at $\Delta_c = +1\Gamma$ (denoted $\delta_{\text{peak},\phi,+}$) is negative and non-negligible according to Eq. (A2). On the other hand, since the value of $\phi_{\delta=0}$ in Fig. 3(f) is very little, the shift of the EIT peak position due to $\phi_{\delta=0}$ at $\Delta_c = -1\Gamma$ (denoted $\delta_{\text{peak},\phi,-}$) is nearly zero according to Eq. (A2).

The frequency shifts due to above two effects are summarized as $\delta_{\text{peak},\gamma,+} > 0$, $\delta_{\text{peak},\gamma,-} < 0$, $\delta_{\text{peak},\phi,+} < 0$, $\delta_{\text{peak},\phi,-} \approx 0$, and $|\delta_{\text{peak},\gamma,-}| > |\delta_{\text{peak},\gamma,+}| \approx |\delta_{\text{peak},\phi,+}|$. Combining the two effects, we obtain the results of net frequency shift of the EIT peak in the followings: $\delta_{\text{peak},\gamma,+} + \delta_{\text{peak},\phi,+} \approx 0$ at $\Delta_c = +1\Gamma$, and $\delta_{\text{peak},\gamma,-} + \delta_{\text{peak},\phi,-} \approx \delta_{\text{peak},\gamma,-} (< 0)$ at $\Delta_c = -1\Gamma$. Hence, the shift of the EIT peak position at $\Delta_c = +1\Gamma$ is not observable in Fig. 3(a), and that at $\Delta_c = -1\Gamma$ is obvious and negative in Fig. 3(c).

-
- [1] M. D. Lukin, M. Fleischhauer, R. Cote, L. M. Duan, D. Jaksch, J. I. Cirac, and P. Zoller, Phys. Rev. Lett. **87**, 037901 (2001).
 - [2] D. Tong, S. M. Farooqi, J. Stanojevic, S. Krishnan, Y. P. Zhang, R. Cote, E. E. Eyler, and P. L. Gould, Phys. Rev. Lett. **93**, 063001 (2004).
 - [3] R. Heidemann, U. Raitzsch, V. Bendkowsky, B. Butscher, R. Löw, L. Santos, and T. Pfau, Phys. Rev. Lett. **99**, 163601 (2007).
 - [4] M. Saffman, T. G. Walker, and K. Mølmer, Rev. Mod. Phys., **82**, 2313 (2010).
 - [5] G. Bannasch, T. C. Killian, and T. Pohl, Phys. Rev. Lett. **110**, 253003 (2013).
 - [6] M. Fleischhauer, A. Imamoglu, and J. P. Marangos, Rev. Mod. Phys. **77**, 633 (2005).
 - [7] Y.-F. Chen, C.-Y. Wang, S.-H. Wang, and I. A. Yu, Phys. Rev. Lett. **96**, 043603 (2006).
 - [8] Z. B. Wang, K.-P. Marzlin, and B. C. Sanders, Phys. Rev. Lett. **97**, 063901 (2006).
 - [9] S. J. Li, X. D. Yang, X. M. Cao, C. H. Zhang, C. D. Xie, and H. Wang, Phys. Rev. Lett. **101**, 073602 (2008).
 - [10] B.-W. Shiao, M.-C. Wu, C.-C. Lin, and Y.-C. Chen, Phys. Rev. Lett. **106**, 193006 (2011).
 - [11] V. Venkataraman, K. Saha, and L. Gaeta, Nat. Photonics **7**, 138 (2012).
 - [12] Y.-H. Chen, M.-J. Lee, W. Hung, Y.-C. Chen, Y.-F. Chen, and I. A. Yu, Phys. Rev. Lett. **108**, 173603 (2012).
 - [13] A. Feizpour, M. Hallaji, G. Dmochowski, and A. M. Steinberg, Nat. Phys. **11**, 905 (2015).
 - [14] Z.-Y. Liu, Y.-H. Chen, Y.-C. Chen, H.-Y. Lo, P.-J. Tsai, I. A. Yu, Y.-C. Chen, and Y.-F. Chen, Phys. Rev. Lett. **117**, 203601 (2016).
 - [15] M. Fleischhauer and M. D. Lukin, Phys. Rev. Lett. **84**, 5094 (2000).
 - [16] M. Fleischhauer and M. D. Lukin, Phys. Rev. A **65**, 022314 (2002).
 - [17] J. D. Pritchard, D. Maxwell, A. Gauguier, K. J. Weatherill, M. P. A. Jones, and C. S. Adam, Phys. Rev. Lett.

- 105**, 193603 (2010).
- [18] D. Petrosyan, J. Otterbach, and M. Fleischhauer, *Phys. Rev. Lett.* **107**, 213601 (2011).
- [19] A. V. Gorshkov, J. Otterbach, M. Fleischhauer, T. Pohl, and M. D. Lukin, *Phys. Rev. Lett.* **107**, 133602 (2011).
- [20] T. Peyronel, O. Firstenberg, Q.-Y. Liang, S. Hofferberth, A. V. Gorshkov, T. Pohl, M. D. Lukin, and V. Vuletić, *Nature (London)* **488**, 57 (2012).
- [21] S. Baur, D. Tiarks, G. Rempe, and S. Dürr, *Phys. Rev. Lett.* **112**, 073901 (2014).
- [22] H. Gorniaczyk, C. Tresp, J. Schmidt, H. Fedder, and S. Hofferberth, *Phys. Rev. Lett.* **113**, 053601 (2014).
- [23] D. Tiarks, S. Baur, K. Schneider, S. Dürr, and G. Rempe, *Phys. Rev. Lett.* **113**, 053602 (2014).
- [24] M. Moos, M. Höning, R. Unanyan, and M. Fleischhauer, *Phys. Rev. A* **92**, 053846 (2015).
- [25] D. Tiarks, S. Schmidt, G. Rempe, and S. Dürr, *Sci. Adv.* **2**, e1600036 (2016).
- [26] O. Firstenberg, C. S. Adams, and S. Hofferberth, *J. Phys. B* **49**, 152003 (2016).
- [27] H. Bernien, S. Schwartz, A. Keesling, H. Levine, A. Omran, H. Pichler, S. Choi, A. S. Zibrov, M. Endres, M. Greiner, V. Vuletić, and M. D. Lukin, *Nature (London)* **551**, 579 (2017).
- [28] J. Ruseckas, I. A. Yu, and G. Juzeliūnas, *Phys. Rev. A* **95**, 023807 (2017).
- [29] H. Levine, A. Keesling, A. Omran, H. Bernien, S. Schwartz, A. S. Zibrov, M. Endres, M. Greiner, V. Vuletić, and M. D. Lukin, *Phys. Rev. Lett.* **121**, 123603 (2018).
- [30] F. Ripka, H. Kübler, R. Löw, and T. Pfau, *Science* **362**, 446 (2018).
- [31] H. Levine, A. Keesling, G. Semeghini, A. Omran, T. T. Wang, S. Ebadi, H. Bernien, M. Greiner, V. Vuletić, H. Pichler, and M. D. Lukin, *Phys. Rev. Lett.* **123**, 170503 (2019).
- [32] D. Tiarks, S. Schmidt-Eberle, T. Stolz, G. Rempe, and S. Dürr, *Nat. Phys.* **15**, 124 (2019).
- [33] S. Chandrasekhar, *Rev. Mod. Phys.* **15**, 1 (1943).
- [34] B. Kim, K.-T. Chen, S.-S. Hsiao, S.-Y. Wang, K.-B. Li, J. Ruseckas, G. Juzeliūnas, T. Kirova, M. Auzinsh, Y.-C. Chen, Y.-F. Chen, and I. A. Yu, to be posted on arXiv.
- [35] M. Fleischhauer, J. Otterbach, and R. G. Unanyan, *Phys. Rev. Lett.* **101**, 163601 (2008).
- [36] J. Kasprzak, M. Richard, S. Kundermann, A. Baas, P. Jeambrun, J. M. J. Keeling, F. M. Marchetti, M. H. Szymańska, R. André, J. L. Staehli, V. Savona, P. B. Littlewood, B. Deveaud, and L. S. Dang, *Nature (London)* **443**, 409 (2006).
- [37] R. Balili, V. Hartwell, D. Snoke, L. Pfeiffer, and K. West, *Science* **316**, 1007 (2007).
- [38] H. Deng, H. Haug, and Y. Yamamoto, *Rev. Mod. Phys.* **82**, 1489 (2010).
- [39] T. G. Walker and M. Saffman, *Phys. Rev. A* **77**, 032723 (2008).